

Supporting information

Exceptional Control of Catalytic Hierarchical Carbon Supported Transition Metal Nanoparticles using Metal-Organic Framework Templates

Jongsik Kim, Gregory T. Neumann, Nicholas D. McNamara, and Jason C. Hicks*

Department of Chemical and Biomolecular Engineering, University of Notre Dame, 182, Fitzpatrick Hall, Notre Dame, IN, 46556, USA.

*Fax: (+1) 574-631-8366; Tel: (+1) 574-631-1334; E-mail: jhicks3@nd.edu

Contents

Table S1	3
Table S2	4
Table S3	5
Fig. S1	6
Fig. S2	7
Fig. S3	8
Fig. S4	9
Fig. S5	10
Fig. S6	11
Fig. S7	12

<i>Fig. S8</i>	13
<i>Fig. S9</i>	14
<i>Fig. S10</i>	15
<i>Fig. S11</i>	16
<i>Fig. S12</i>	17
<i>Fig. S13</i>	18
<i>Fig. S14</i>	19
<i>Fig. S15</i>	20
<i>Fig. S16</i>	21
<i>Fig. S17</i>	22
<i>Fig. S18</i>	23
<i>Fig. S19</i>	24
<i>Fig. S20</i>	25
<i>Fig. S21</i>	26
<i>Fig. S22</i>	27
<i>Fig. S23</i>	28

Table S1 Physical properties of desolvated IRMOF-3, M/IRMOF-3, desolvated IRMOF-1, and M/IRMOF-1 materials.

material	S _{NLDFT} (m ² /g) ^a	V _{micro} (cm ³ /g) ^a	V _{meso} (cm ³ /g) ^a	V _{pore} (cm ³ /g) ^{a,b}	S _{BET} (m ² /g) ^c	V _{micro} (cm ³ /g) ^{c,d}	V _{meso} (cm ³ /g) ^{c,e}	V _{pore} (cm ³ /g) ^{b,c}
desolvated IRMOF-3-I	900	0.44	0.39	0.83	980	0.46	0.42	0.88
desolvated IRMOF-3-II	1240	0.70	0.28	0.98	1500	0.7	0.21	0.91
Ru/IRMOF-3 ^f	460	0.17	0.34	0.51	420	0.18	0.36	0.54
W/IRMOF-3 ^f	430	0.16	0.35	0.51	400	0.16	0.37	0.53
V/IRMOF-3 ^g	840	0.40	0.22	0.62	890	0.41	0.23	0.64
Ti/IRMOF-3 ^f	340	0.13	0.23	0.36	320	0.14	0.25	0.39
desolvated IRMOF-1	1090	0.37	0.07	0.44	800	0.39	0.01	0.40
Ru/IRMOF-1 ^h	370	0.14	0.06	0.20	330	0.14	0.05	0.19
W/IRMOF-1 ^h	400	0.16	0.03	0.19	360	0.17	0.02	0.19
V/IRMOF-1 ^h	810	0.28	0.02	0.30	610	0.30	0.02	0.32
Ti/IRMOF-1 ^h	690	0.28	0.02	0.30	600	0.29	0.02	0.31

^a by non-localized density functional theory (NLDFT). ^b V_{pore} = V_{micro} + V_{meso}. ^c by BET theory. ^d by t-plot equation. ^e by BJH method using N₂ desorption isotherm. ^f prepared using IRMOF-3-I. ^g prepared using IRMOF-3-II. ^h prepared using same molar ratio of metal precursor to organic linker as those of corresponding M/IRMOF-3.

Table S2 Molar ratios of metal to organic linker for M/IRMOF-3, M/IRMOF-1-C, and M/IRMOF-1 materials obtained via ICP-OES.

	M/IRMOF-3 ^a	M/IRMOF-1-C ^a	M/IRMOF-1 ^{b,c}
Ru	0.014	0.001	0.014
W	0.015	0.001	0.015
V	0.010	0.001	0.010
Ti	0.040	0.002	0.040

^a prepared via PSM. ^b prepared via IMP. ^c prepared using same molar ratio of metal precursor to organic linker as those of corresponding M/IRMOF-3.

Table S3 Comparison of surface phases of nitrogen and metal in M/NC₃ materials with those of metal nitride using XPS spectra.

	binding energy (eV)			
	metal in M/NC ₃		metal nitride	
W	N 1s	W 4f _{7/2}	N 1s	W 4f _{7/2}
	n/d ^a	31.8 (1.1 % ^b)	397.5	32.7-33.6
V	N 1s	V 2p _{3/2}	N 1	V 2p _{3/2}
	398.7 ^c and 401.1 ^d	513.7 (0.7 % ^b)	397.3	514.2-514.5
Ti	N 1s	Ti 2p _{3/2}	N 1s	Ti 2p _{3/2}
	397.3 ^c and 400.7 ^e	454.9 (1.6 % ^b)	396.5	455.5-456.0

^a not detected. ^b surface composition of metal. ^c pyridinic N functionality. ^d quarternary N functionality. ^e pyrolic N functionality.

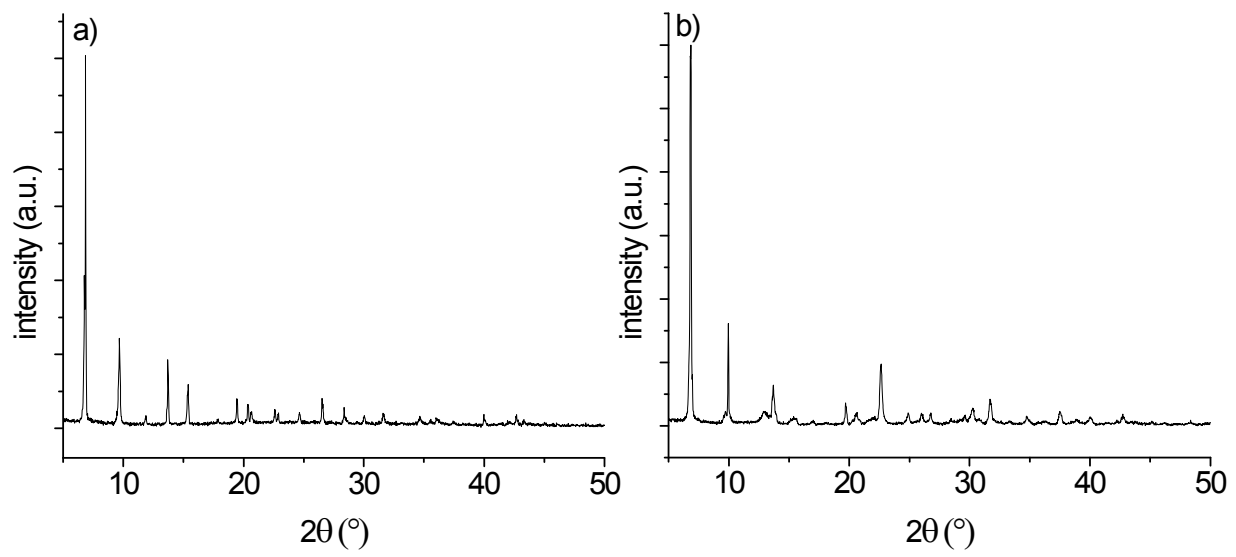


Fig. S1 XRD patterns of a) desolvated IRMOF-3 and b) desolvated IRMOF-1

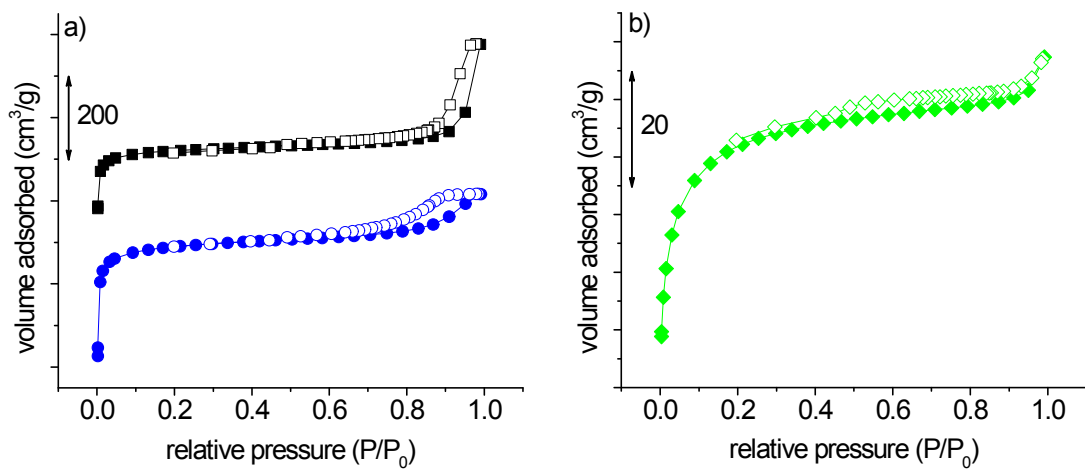


Fig. S2 N₂ isotherms (adsorption (solid symbol) and desorption (empty symbol)) of a) desolvated IRMOF-3-I (square), desolvated IRMOF-3-II (circle), and b) desolvated IRMOF-1 (diamond).

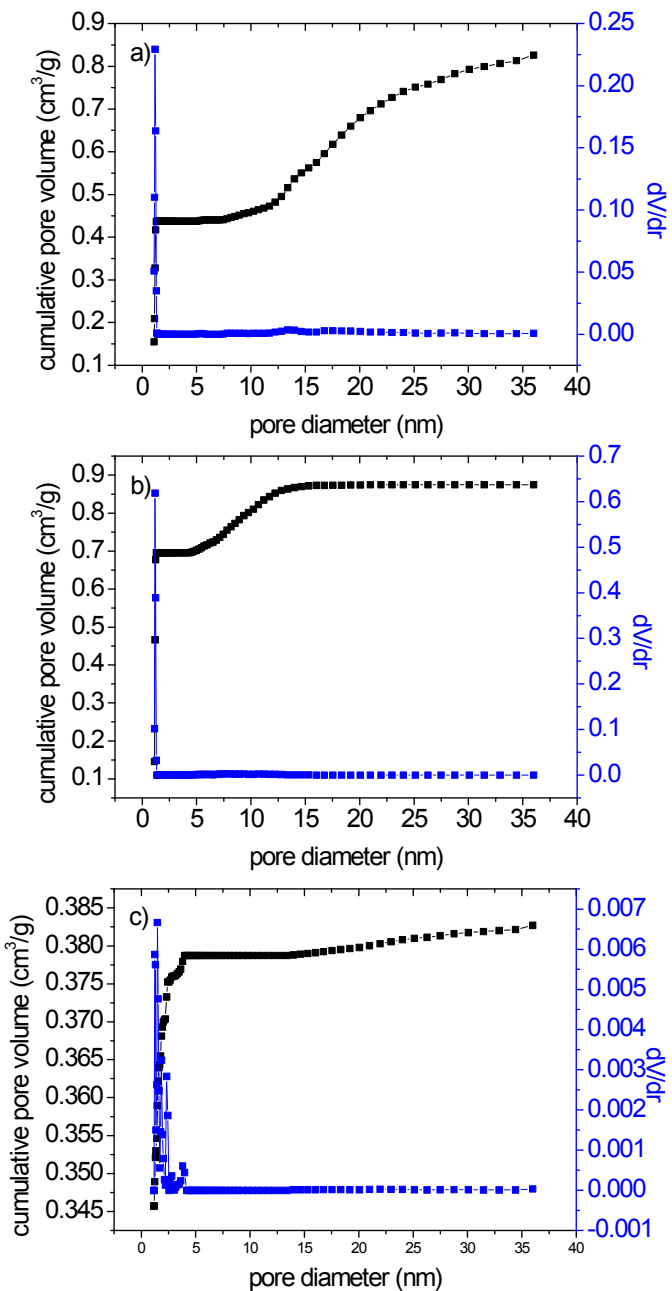


Fig. S3 Pore size distributions of desolvated IRMOF materials obtained based on NLDFT theory: a) IRMOF-3-I, b) IRMOF-3-II, and c) IRMOF-1.

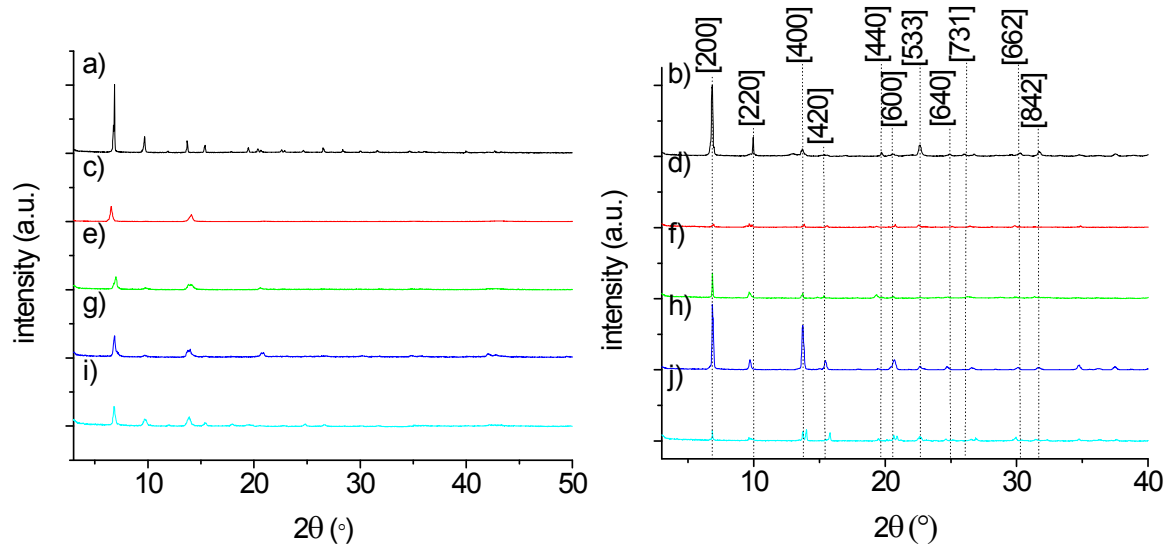


Fig. S4 XRD patterns of a) desolvated IRMOF-3, b) desolvated IRMOF-1, M/IRMOF-3 materials (c for Ru/IRMOF-3; e for WIRMOF-3; g for V/IRMOF-3; I for Ti/IRMOF-3), and M/IRMOF-1 materials (d for Ru/IRMOF-1; f for WIRMOF-1; h for V/IRMOF-1; j for Ti/IRMOF-1).

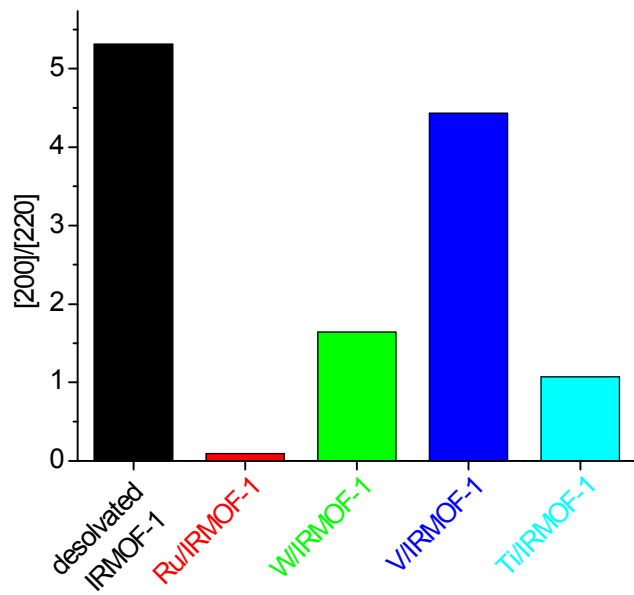


Fig. S5 Area ratio ([200]/[220]) of peaks indicating [200] and [220] in XRD patterns of desolvated IRMOF-1 and M/IRMOF-1 materials.

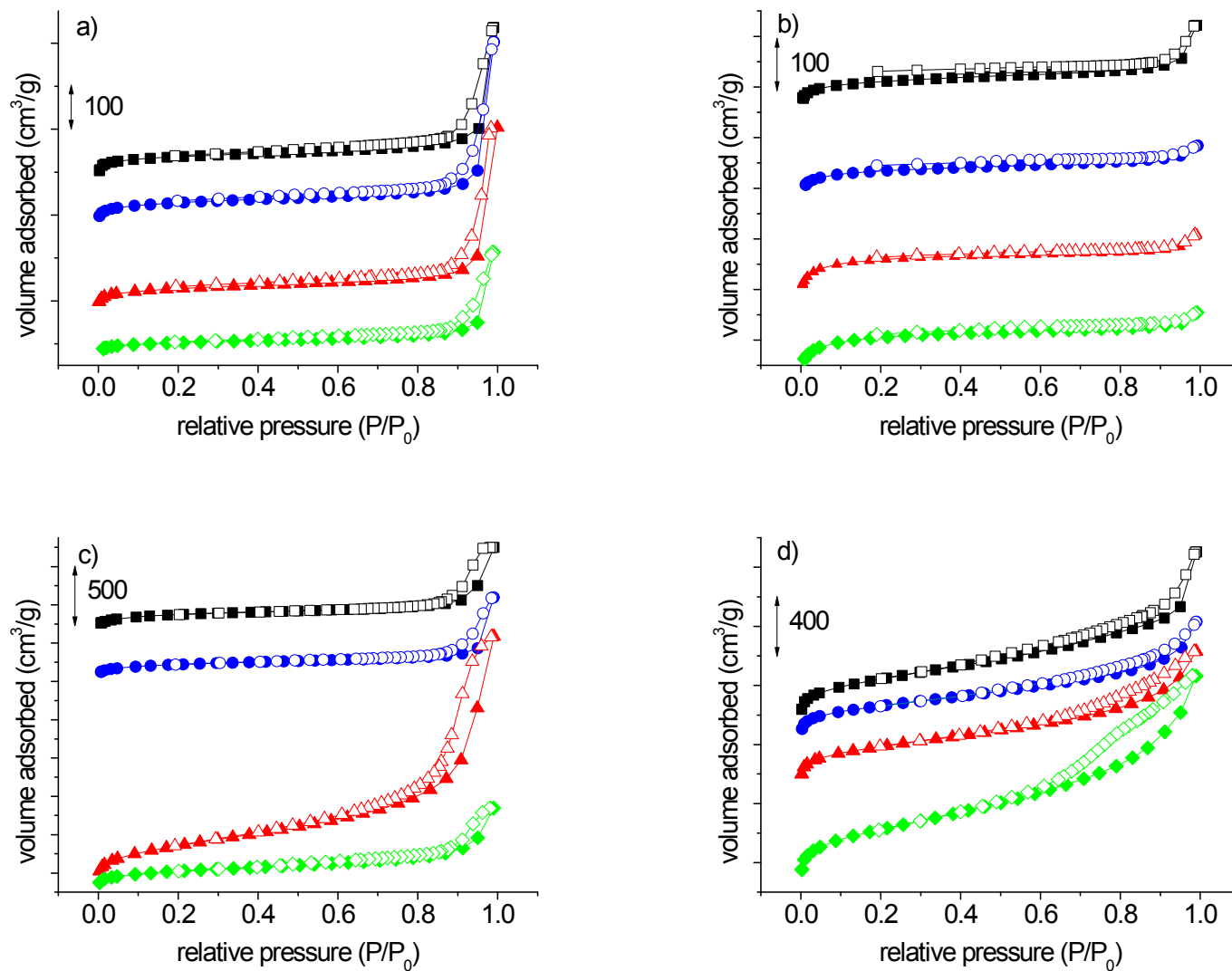


Fig S6 N_2 isotherms (adsorption (solid symbol) and desorption (empty symbol)) of a) M/IRMOF-3, b) M/IRMOF-1, c) M/NC3, and d) M/NC1 materials (square: Ru; circle: W; triangle: V; diamond: Ti).

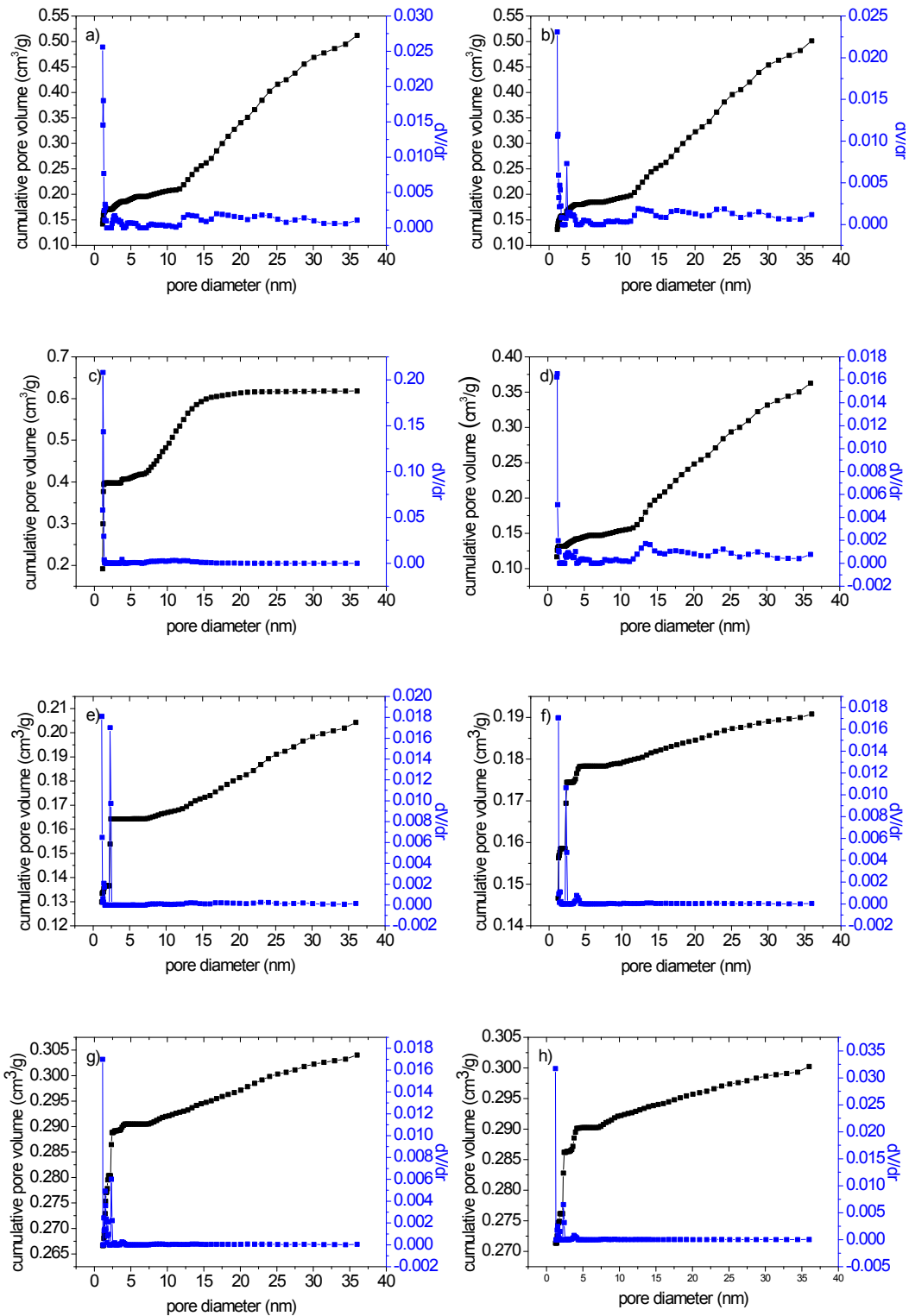


Fig. S7 Pore size distributions of materials obtained based on NLDFT theory: a) Ru/IRMOF-3, b) W/IRMOF-3, c) V/IRMOF-3, d) Ti/IRMOF-3, e) Ru/IRMOF-1, f) W/IRMOF-1, g) V/IRMOF-1, and h) Ti/IRMOF-1.

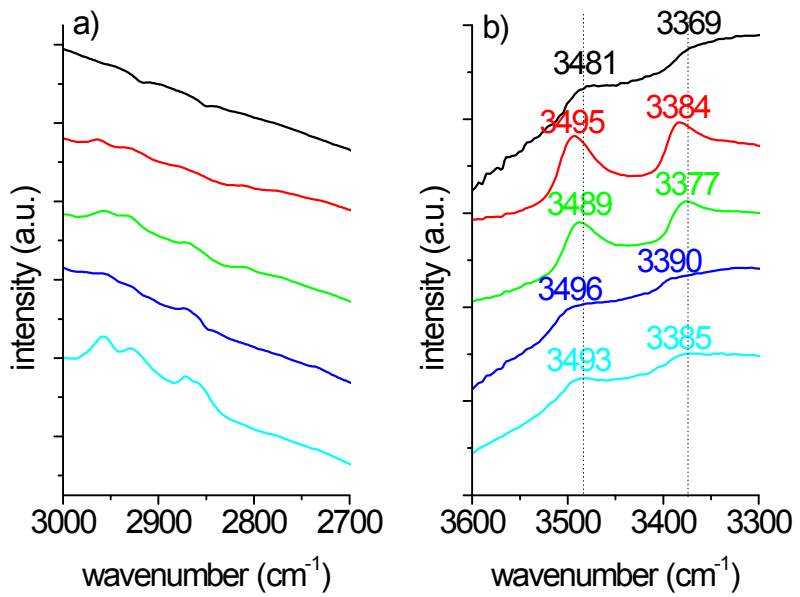


Fig. S8 FT-IR spectra (a and b) of desolvated IRMOF-3 (black) and M/IRMOF-3 materials (red for Ru/IRMOF-3; green for W/IRMOF-3; blue for V/IRMOF-3; cyan for Ti/IRMOF-3). a) and b) showed the typical regions where $\nu(\text{C-H})$ and $\nu(\text{N-H})$ stretching vibrations were observed, respectively.

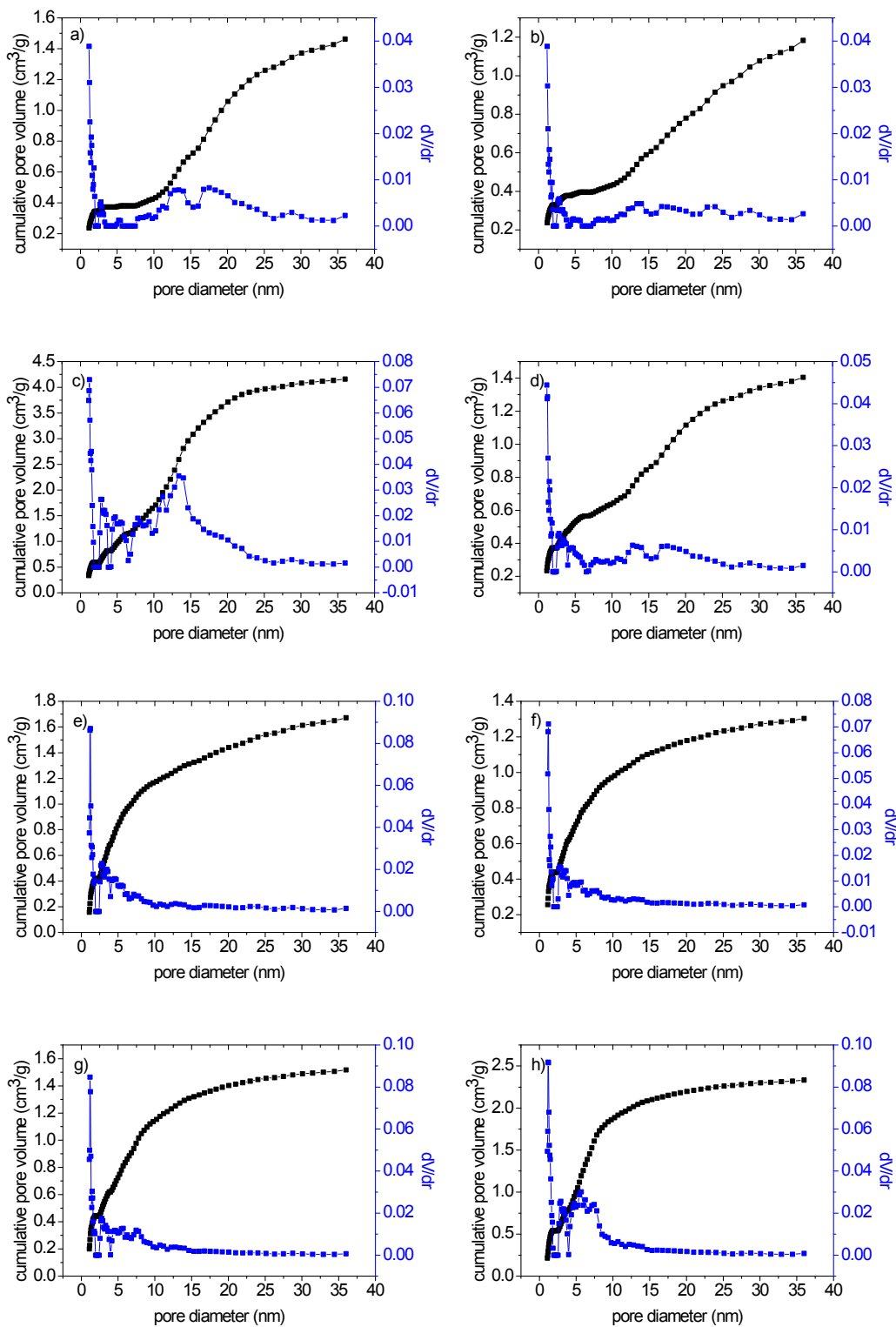


Fig. S9 Pore size distributions of materials obtained based on NLDFT: a) Ru/NC3, b) W/NC3, c) V/NC3, d)

Ti/NC3, e) Ru/NC1, f) W/NC1, g) V/NC1, and h) Ti/NC1.

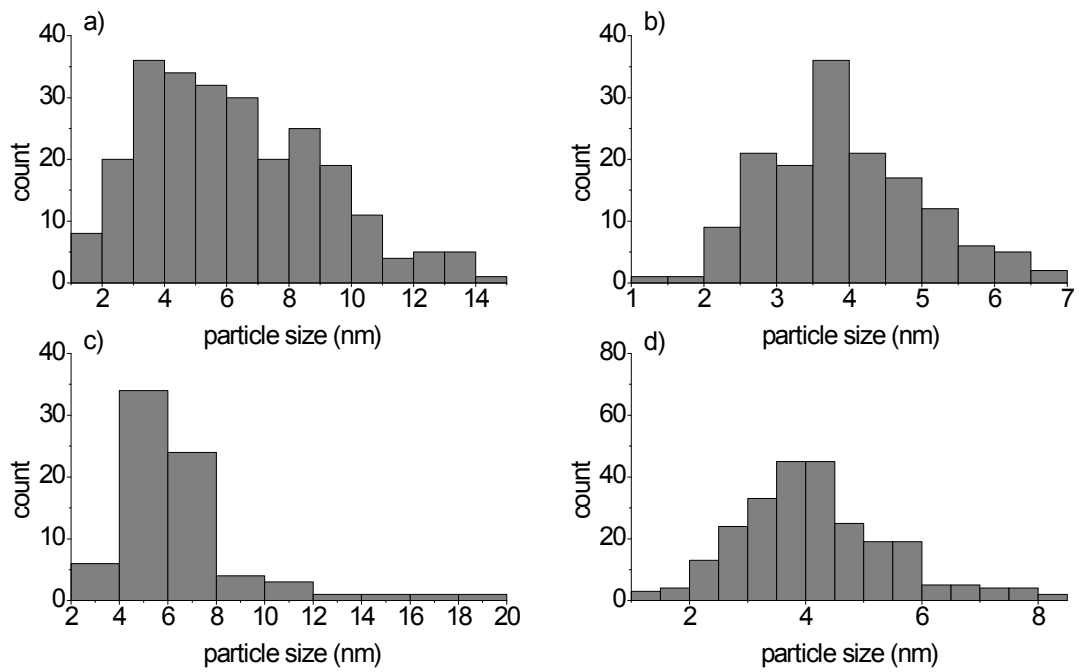


Fig. S10 Particle size distributions of M/NC3 materials (a for Ru/NC3, n=250; b for W/NC3, n=150; c for V/NC3, n=75; d for Ti/NC3, n=250).

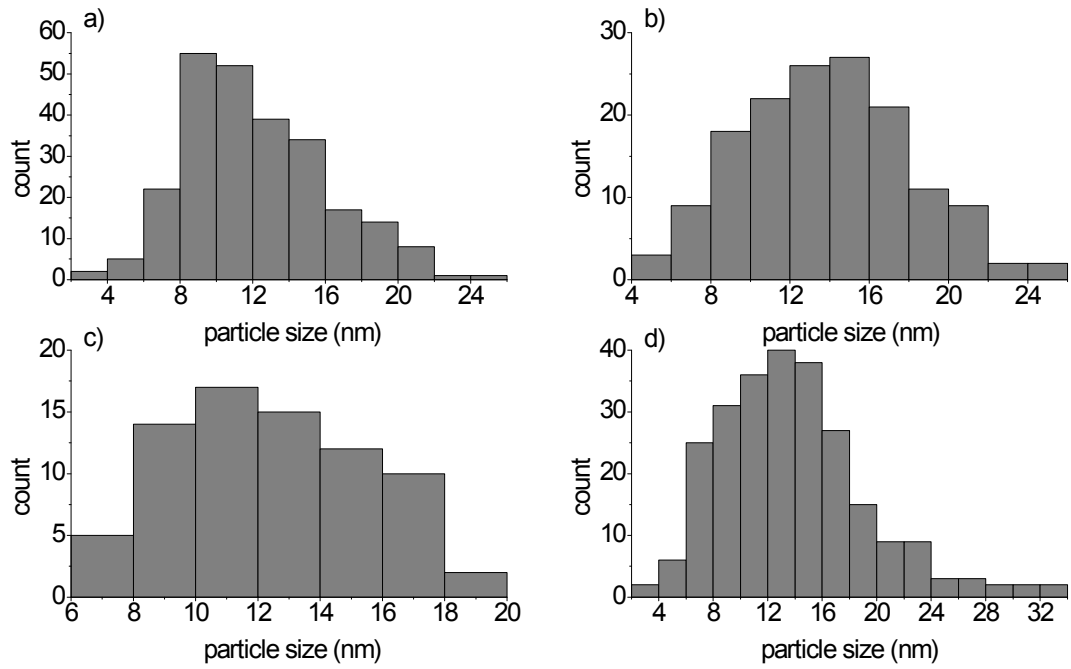


Fig. S11 Particle size distributions of M/NC1 materials (a for Ru/NC1, n=250; b for W/NC1, n=150; c for V/NC1, n=75; d for Ti/NC1, n=250).

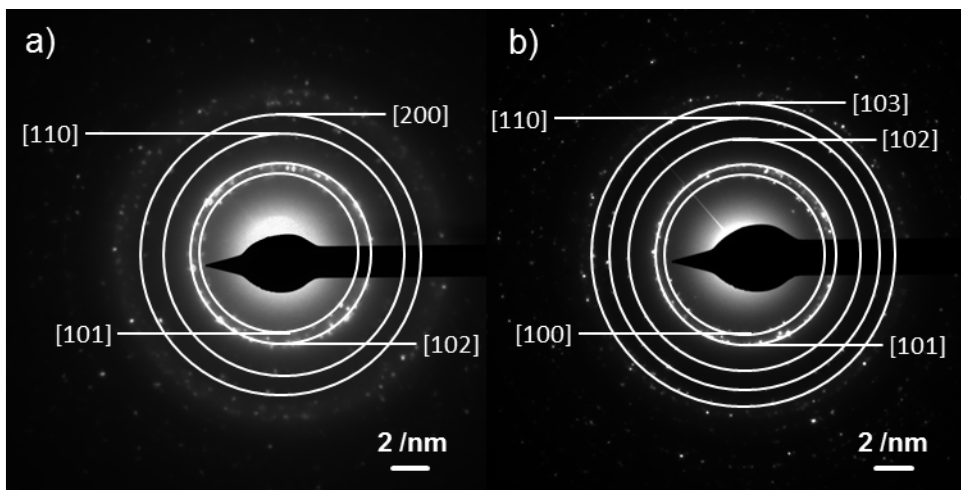


Fig. S12 SAED patterns of a) Ru/NC3 and b) Ru/NC1 materials. Square bracket indicates diffracted crystal plane of metallic Ru.

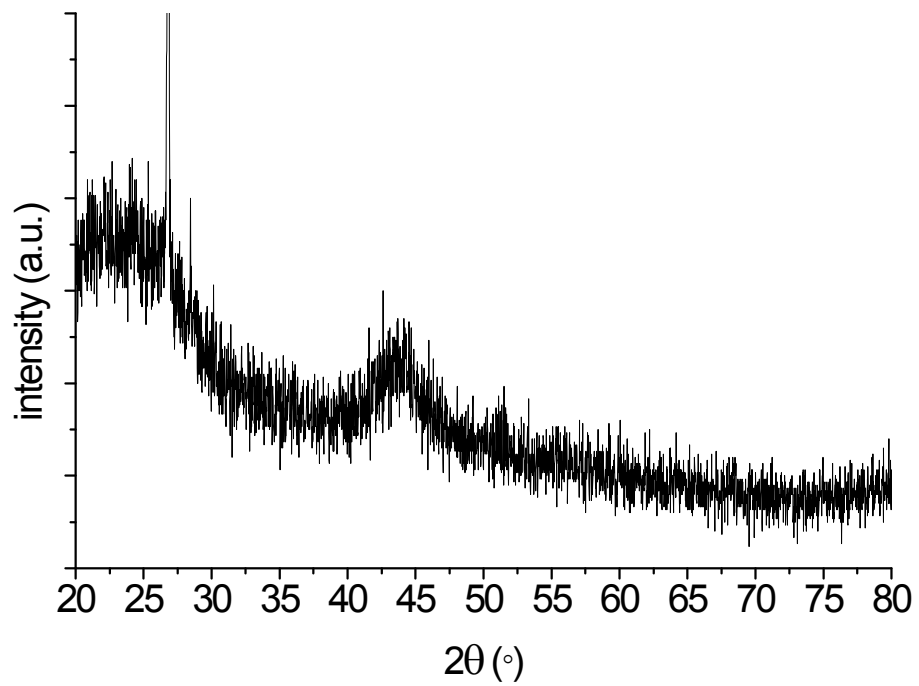


Fig. S13 XRD pattern of Ru/C (commercial).

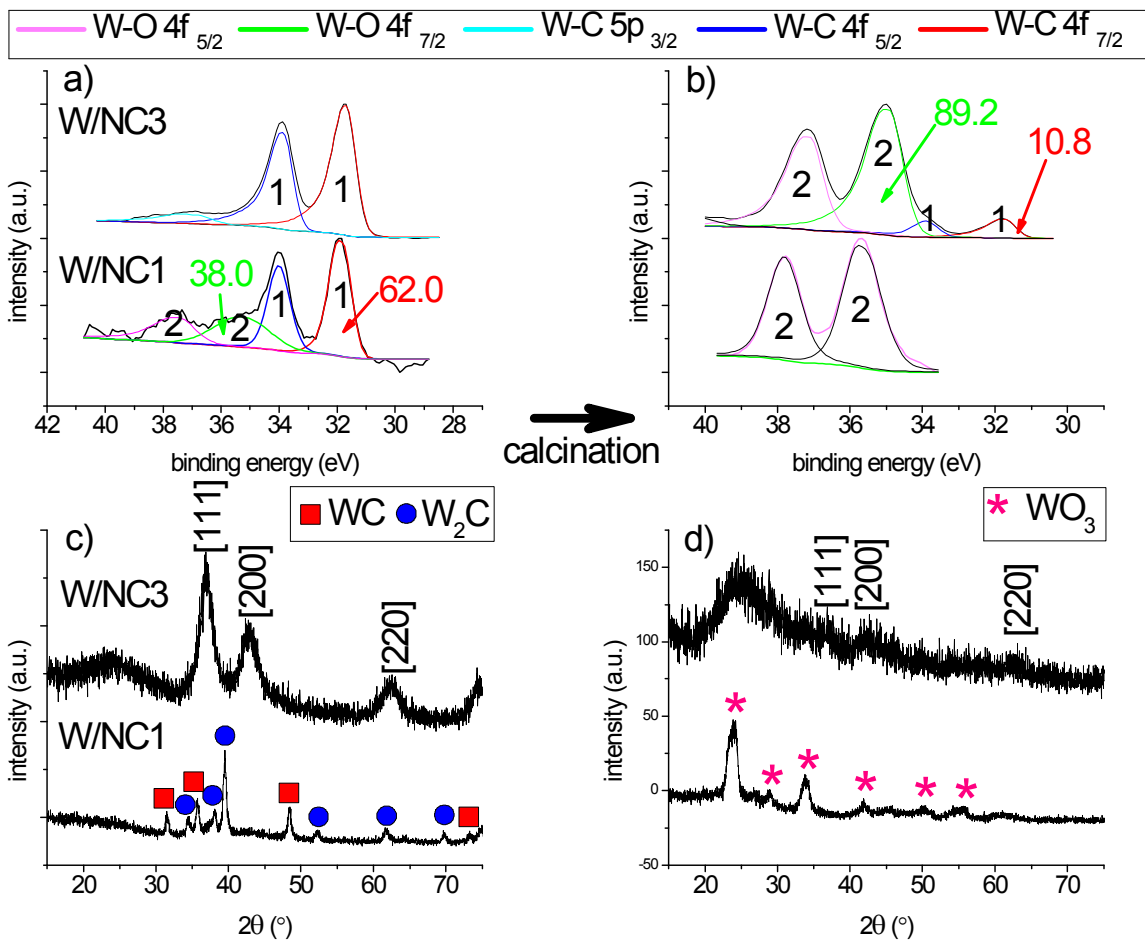


Fig. S14 XPS spectra showing W 4f and W 5p region for W/NC3 and W/NC1 materials a) before and b) after calcination at 450 °C for 1 hour. Fitted regions indicate the following surface phases of tungsten: tungsten carbide (1) and W⁶⁺ (2). Relative abundances of surface phases of tungsten in W/NC3 and W/NC1 materials before and after calcination were also shown as numbers with arrows. XRD patterns of W/NC3 and W/NC1 materials c) before and d) after calcination. Square brackets indicate the bulk phase of WC_{1-x}.

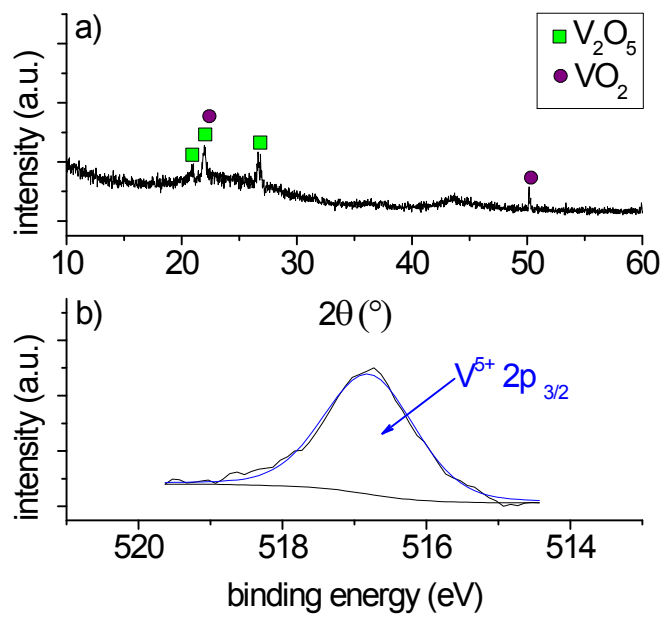


Fig. S15 a) XRD pattern and b) XPS spectrum showing V 2p region of V/AC.

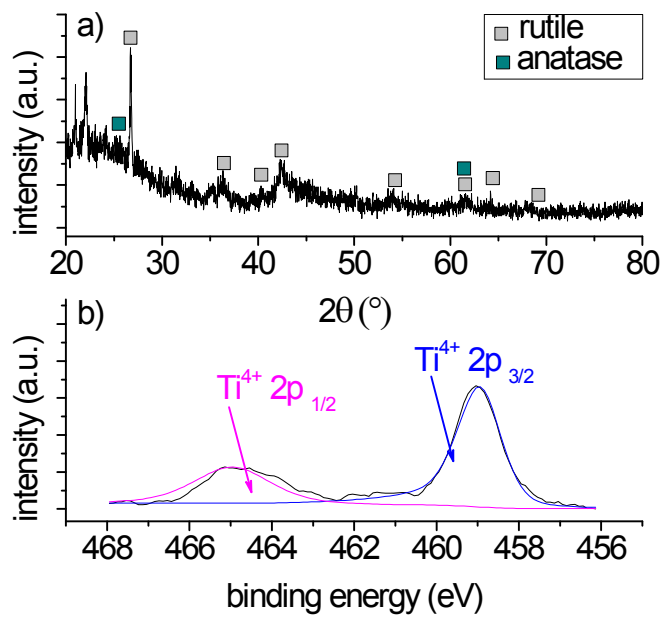


Fig. S16 a) XRD pattern and b) XPS spectrum showing Ti 2p region of Ti/AC.

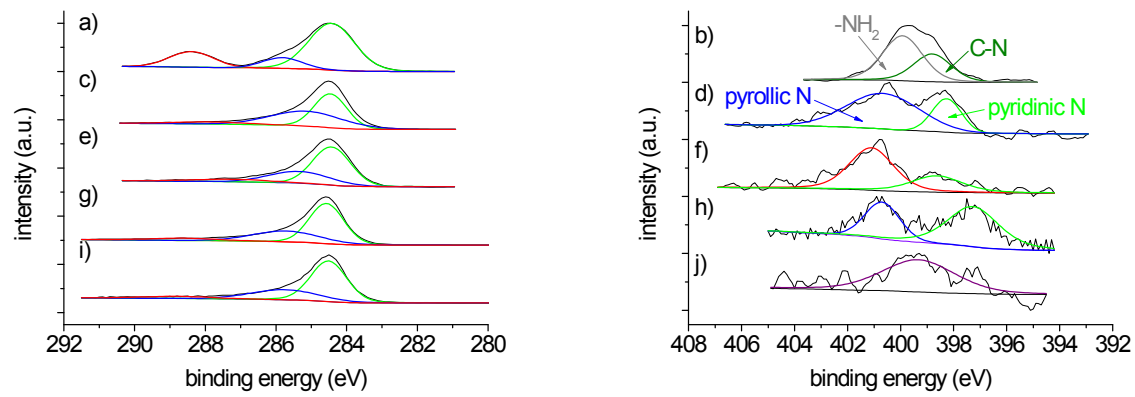


Fig S17 XPS spectra of C 1s (left) and N 1s (right) region for desolvated IRMOF-3 (a, b), NC3 (c, d), W/NC3 (e), V/NC3 (f, g), and Ti/NC3 (h, i), and Ru/NC3 (j).

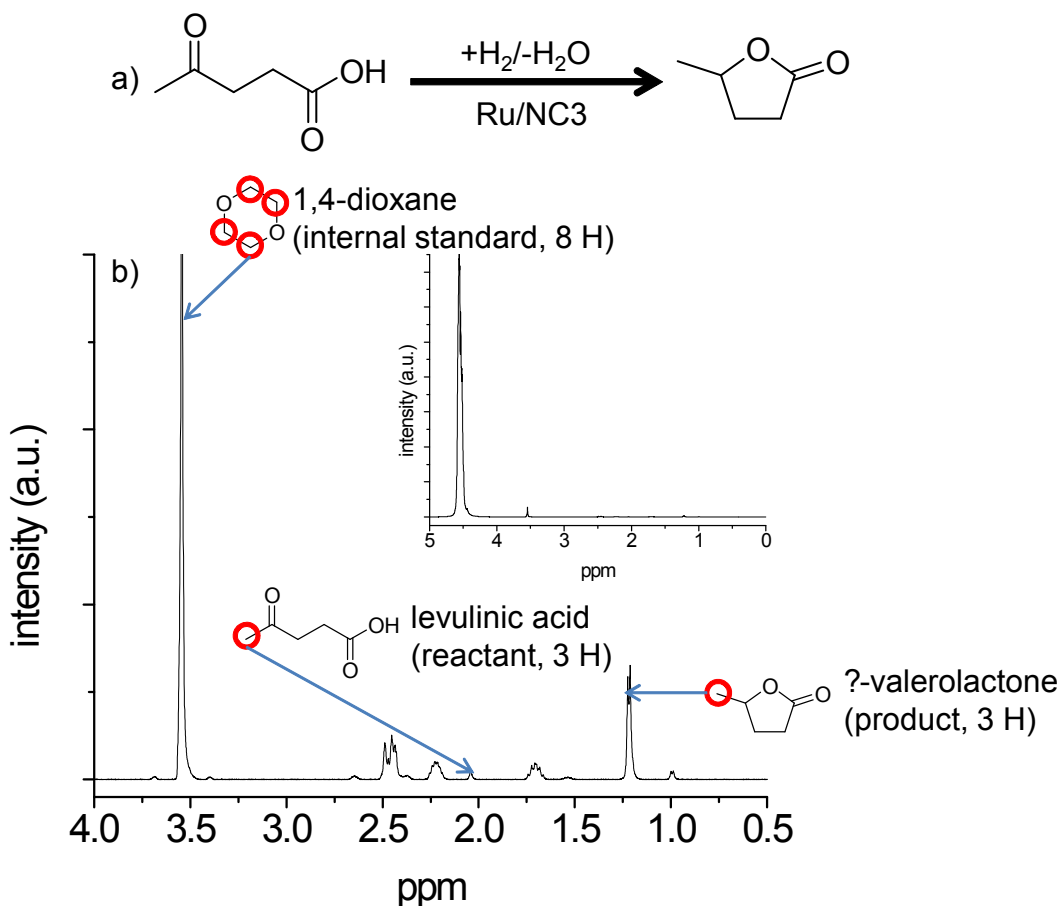


Fig. S18 a) reaction scheme for the liquid phase catalytic hydrogenation of levulinic acid and b) typical ^1H -NMR spectroscopy (solvent: $\text{DMSO}-d_6$) of reaction mixture after reaction in the chemical shift range between 0.5 to 4.0 ppm. Inset: general b) in entire chemical shift region.

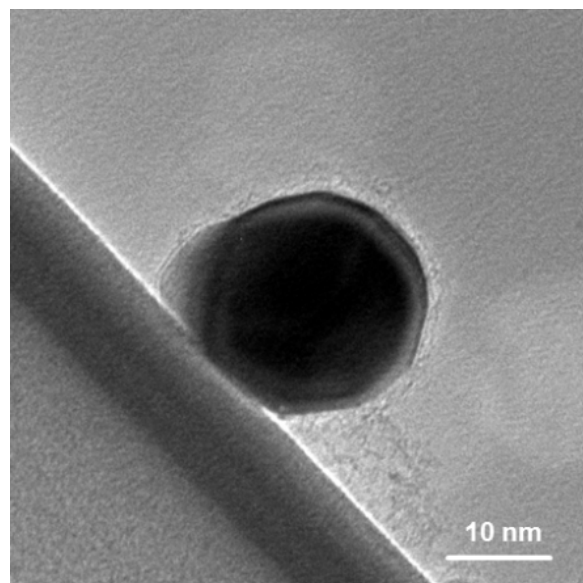


Fig. S19 HRTEM image of carbon-encapsulated Ru nanoparticles in Ru/NC1.

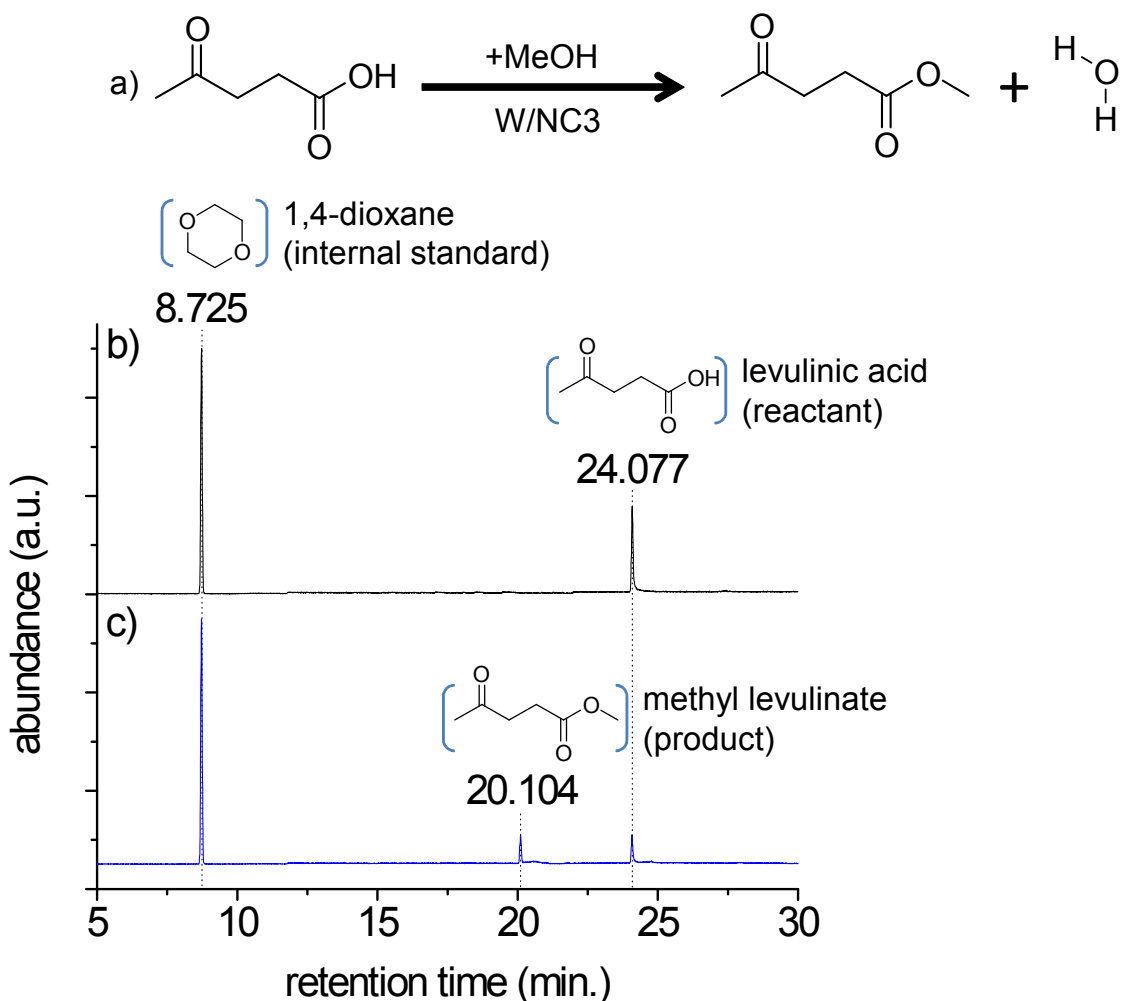


Fig. S20 a) reaction scheme for the liquid phase catalytic esterification of levulinic acid and typical GC-MS results of reaction mixture b) before and c) after reaction.

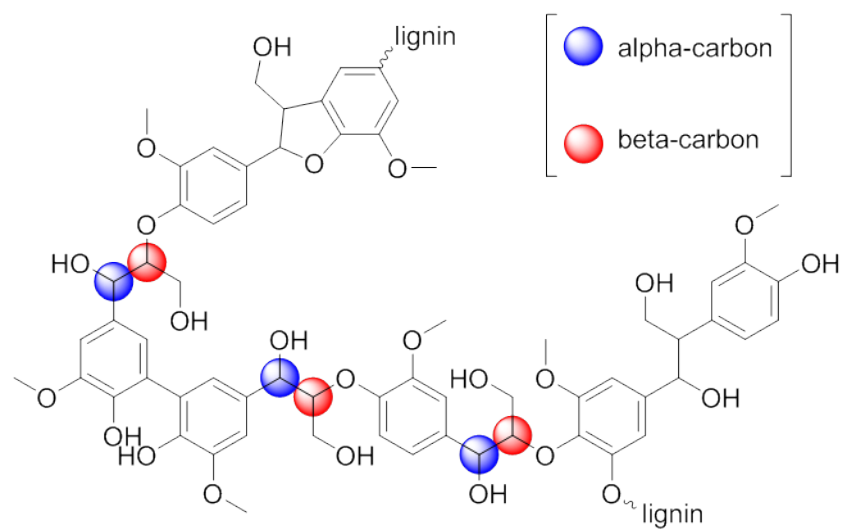


Fig. S21 Representation of lignin in its proposed form in lignocellulosic biomass.

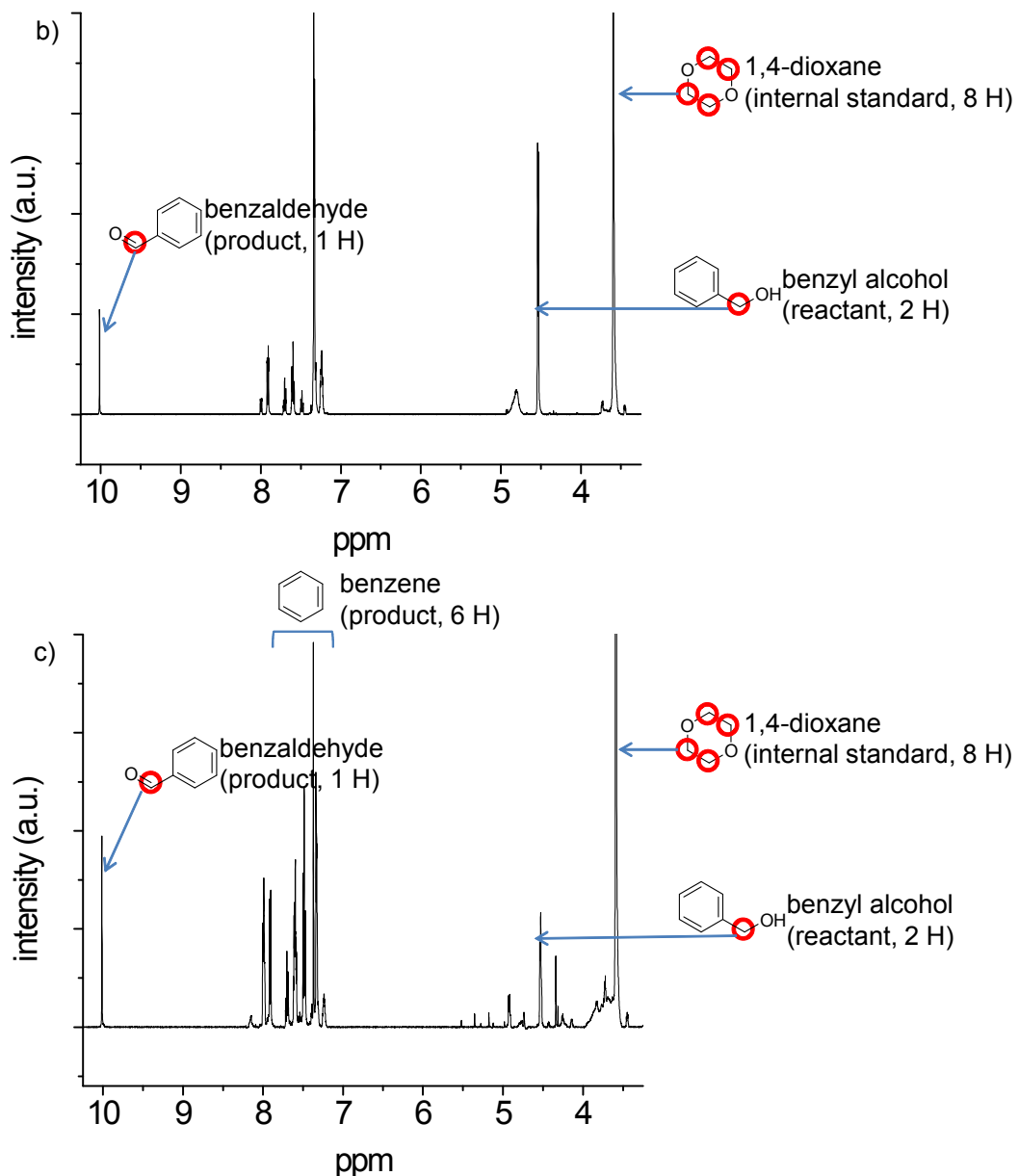
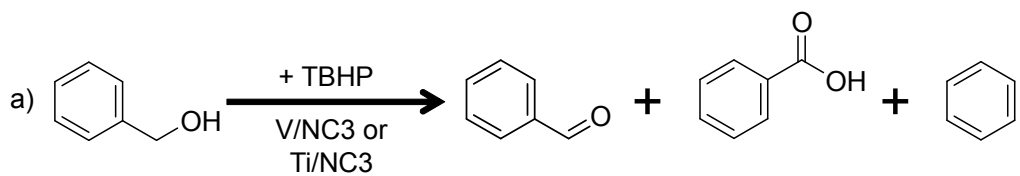


Fig. S22 a) reaction scheme for the liquid phase catalytic oxidation of benzyl alcohol and magnified typical ^1H -NMR spectroscopy (solvent: $\text{DMSO}-d_6$) of reaction mixtures after reaction in the chemical shift range between 3.25 to 10.25 ppm using b) Ti/NC and c) V/NC as catalysts. Inset: general b) and c) in entire chemical shift region.

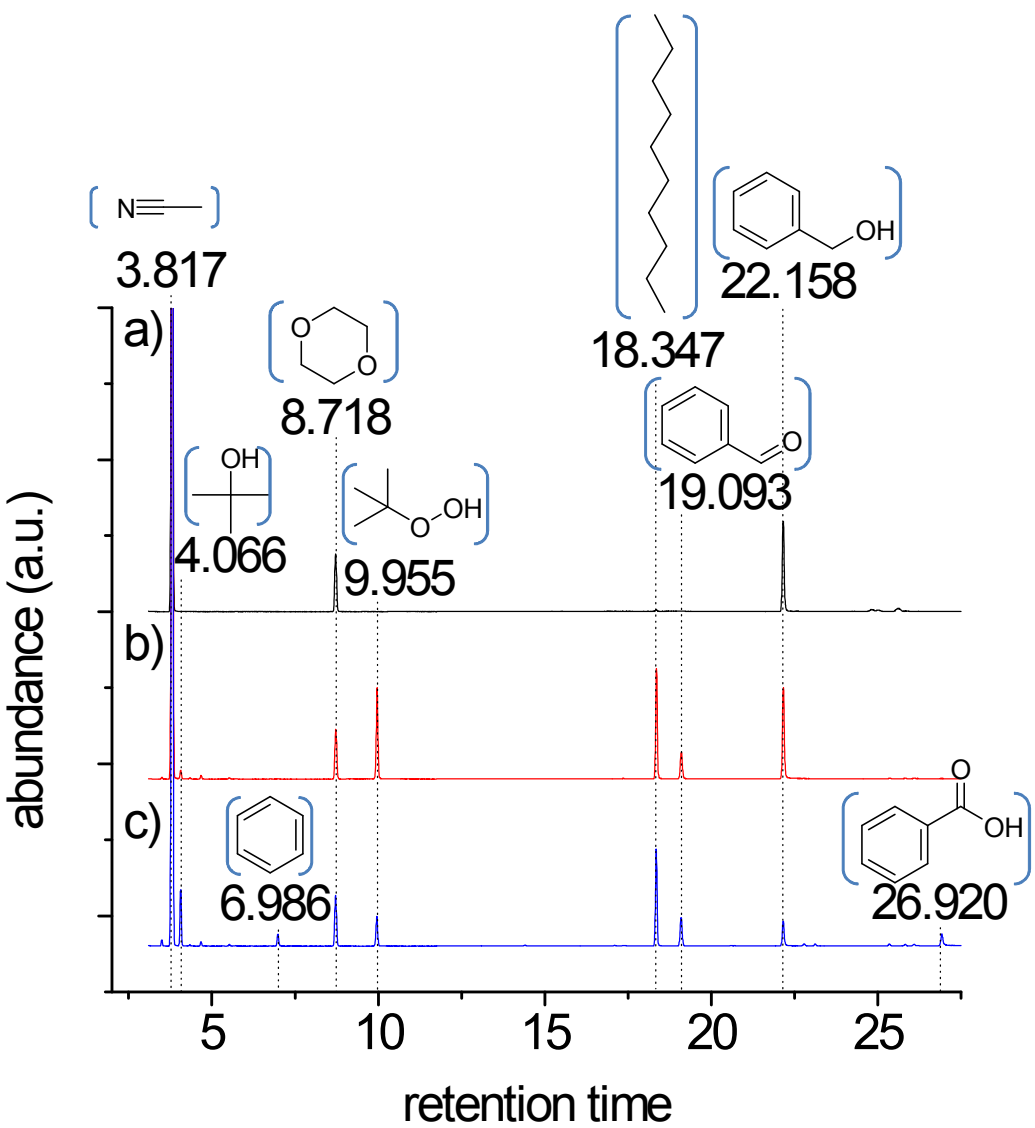


Fig. S23 Typical GC-MS results of reaction mixtures a) before, b) after reaction using Ti/NC, and c) after reaction using V/NC.